Available online at www.sciencedirect.com
ScienceDirect
Acta Materialia 57 (2009) 1290–1299
Acta MATERIALIA
www.elsevier.com/locate/actamat

Zr–Cu–Ni–Al bulk metallic glasses with superhigh glass-forming ability

Y.J. Sun [a], D.D. Qu [a], Y.J. Huang [a], K.-D. Liss [b], X.S. Wei [a], D.W. Xing [a], J. Shen [a,c,*]

[a] School of Materials Science and Engineering, Harbin Institute of Technology, Harbin 150001, China
[b] The Bragg Institute, Australian Nuclear Science and Technology Organisation, Lucas Heights, NSW 2234, Australia
[c] Micro/Nano Technology Research Center, Harbin Institute of Technology, Harbin 150001, China

Received 11 October 2008; received in revised form 4 November 2008; accepted 5 November 2008
Available online 26 December 2008

Abstract

Zr–Cu–Ni–Al quaternary amorphous alloy compositions with varying glass-forming ability are developed by an efficient method of proportional mixing of binary eutectics. The critical diameter of the glassy sample is improved from 6 mm for $Zr_{53}Cu_{18.7}Ni_{12}Al_{16.3}$ to 14 mm for $Zr_{50.7}Cu_{28}Ni_9Al_{12.3}$ by straightforwardly adjusting the eutectic unit's coefficients. The drastic improvement in GFA is attributed to balancing the chemical affinities of the Zr, Cu, Ni and Al components in the melt prior to solidification which makes the precipitation of competing crystalline phases more difficult. As the glass-forming ability increases, the concentration of Cu in the alloys exhibits a same trend. Based on synchrotron radiation high-energy X-ray diffraction analysis and Miracle's structural model, it is envisioned that the substitution of additional Cu atoms for Zr atoms in the investigated alloys stabilizes the efficient cluster packing structure of the amorphous alloys, leading to the pronounced increase in their glass-forming ability.
© 2008 Acta Materialia Inc. Published by Elsevier Ltd. All rights reserved.

Keywords: Bulk metallic glasses; Binary deep eutectic; Glass-forming ability; Structure; PDF analysis

1. Introduction

Due to their extraordinary disordered atomic configuration, bulk metallic glasses (BMGs), also called bulk amorphous alloys, exhibit favorable mechanical properties, such as high strength, high hardness and excellent impact resistance, which are important qualities for engineering and structural materials [1–6]. Among these, Zr-based BMGs have been drawing extensive attention because of their high glass-forming ability (GFA) as well as their outstanding properties. It has previously been reported that the Zr-based glass-forming alloys with a critical diameter of more than 10 mm have been successfully explored in the systems of Zr–Ti–Ni–Cu–Be [7], Zr–(Ag, Cu)–Al [8], Zr–Cu–Ni–Al–Pd [9], and a few other alloys [10–12]. To date, the Zr-based bulk-sized metallic glasses with superior GFA, however, usually contain either a toxic element (e.g., Be) [7] or precious metals (e.g., Ag and Pd) [8,9], which severely hinders widespread practical applications for such advanced materials. Therefore, it is not only of fundamental scientific importance but also of great practical importance to develop Zr-based bulk glassy alloys free of poisonous and/or noble elements with exceptionally high GFA.

A metallic glass can be fabricated if a melted alloy is cooled sufficiently rapidly to suppress crystallization [13]. However, critical cooling rates for glass formation are usually very high (typically above 10^4 K s^{-1}). The necessity of such a high cooling rate restricts the possible amorphous alloy forms to ribbon, powder, or wire [14,15]. As is known, the GFA for BMGs is sensitive to the alloy composition. Numerous efforts have therefore focused on finding BMGs [16–22]. A significant amount of experimental trial and error is required to optimize these alloys, but it is still a challenge to find good glass formers in an efficient and straightforward manner.

The reduced glass transition temperature, T_{rg} ($=T_g/T_l$, where T_g and T_l are the glass transition temperature and

* Corresponding author. Address: School of Materials Science and Engineering, Harbin Institute of Technology, Harbin 150001, China. Tel.: +86 451 86403196.
E-mail address: junshen@hit.edu.cn (J. Shen).

1359-6454/$34.00 © 2008 Acta Materialia Inc. Published by Elsevier Ltd. All rights reserved.
doi:10.1016/j.actamat.2008.11.007

the liquidus temperature, respectively), proposed by Turnbull based on the consideration of bypassing crystal nucleation [23], has been often quoted to evaluate the GFA of amorphous materials. This criterion predicts that glasses form preferentially in alloy systems with "deep eutectic" features upon cooling the liquid [23–25]. For binary alloys, it is relatively easy to locate their eutectic compositions according to well-established phase diagrams. For multi-component alloy systems, however, the useful data of phase diagrams are very limited.

Recently, Shen and co-workers [26,27] proposed an alternative approach to directly predict bulk glass-forming compositions. This straightforward method, based on "proportional mixing of binary eutectics", suggests that multi-component glass-forming compositions could be primarily determined by mixing binary eutectics of the constituent elements in the proper ratios [26]. Usually, there are two features associated with these binary eutectics: relatively low eutectic temperatures and line compound products from eutectic reactions. Several Zr-based [26,27], Ni-based [28] and Cu-based [29] bulk metallic glasses have been successfully explored based on this approach, demonstrating the validity of searching for BMG compositions with high GFA.

In this paper, amorphous alloys in the Zr–Cu–Ni–Al system were designed through the proportional mixing of the binary eutectics $Zr_{44}Cu_{56}$, $Zr_{51}Al_{49}$ and $Zr_{64}Ni_{36}$. The ratios of these binary eutectics were adjusted in order to suppress the competing crystalline phases in the amorphous matrix which normally precipitate during cooling of the molten liquid [30]. Three new Zr–Cu–Ni–Al alloys with high GFA were obtained by varying the ratios of the constituent elements. A quaternary Zr–Cu–Ni–Al alloy, i.e., $Zr_{50.7}Cu_{28}Ni_9Al_{12.3}$, with a critical diameter of 14 mm was achieved after only a few experimental trials. The atomic packing in the resultant alloys was obtained by synchrotron radiation high-energy X-ray diffraction (HEXRD). The GFA of the Zr-based amorphous alloys are interpreted on the basis of phase selection and Miracle's structural model [31,32].

2. Experimental

Ingots of quaternary Zr–Cu–Ni–Al alloys were prepared by arc melting the mixtures of highly pure constituent elements Zr (99.5%), Cu (99.9%), Ni (99.9%) and Al (99.99%) in a Ti-gettered argon atmosphere. In order to ensure the homogeneity of the composition, each ingot was remelted at least four times, followed by casting the melted alloys into a copper mold to form rod-shaped samples with various diameters.

The structure of the as-cast samples was characterized by X-ray diffraction (XRD) with Cu Kα radiation (D/MAX-RB diffractometer), scanning electron microscopy (SEM) performed on a Hitachi S-4700 machine, and transmission electron microscopy (TEM) carried out on a Philips CM200 device at a voltage of 200 kV. The thin foil samples for TEM observation were prepared by two-jet electropolishing. Thermal analysis was performed using differential scanning calorimetry (DSC, Perkin–Elmer DSC7) and differential thermal analysis (DTA, Perkin–Elmer DTA7) at a constant heating rate of 0.33 K s^{-1} under a flowing purified argon atmosphere.

The as-cast samples of 3 mm diameter were studied by atomic pair distribution function (PDF) analysis using HEXRD at the beamline ID15B of the European Synchrotron Radiation Facility (ESRF) in France [33,34]. The incident X-ray beam parameters, energy, wavenumber and wavelength were 87.77 keV, 47.48 $Å^{-1}$ and 0.1413 Å, respectively, and the beam size was shaped to 1×1 mm^2. A two-dimensional flat panel pixel detector (Thales Pixium 4700 model) with a pixel size of 0.154 mm was placed in the 245 mm forward direction in order to record the diffraction pattern with high momentum transfers Q. The 2D experimental data were reduced using the package dataRring [35] to obtain the 1D intensity distribution $I(Q)$ up to a usable momentum transfer of 20 $Å^{-1}$. Then, the scattering function $S(Q)$ and its PDF obtained by Fourier transformation were achieved using the program RAD [36]. The momentum transfer Q, allowing to compare directly scattering patterns from XRD and HEXRD in Figs. 1–3a, 5 and 6 on an absolute scale, is the length of the scattering vector and directly related to the scattering angle, 2θ, and the wavelength, λ, by the following equation:

$$Q = 4\pi \sin(\theta)/\lambda \tag{1}$$

3. Results

It has been demonstrated by numerous experiments that the primary crystalline phases for Zr–Cu–Ni–Al amorphous alloy systems are mainly Zr–Cu, Zr–Ni and Zr–Al intermetallics [37–39]. Such intermetallics can always be treated as competing phases to the glassy phase in the alloy system. In a glass-forming liquid, once the driving forces for precipitation of all competing crystalline phases are balanced, then the ability to hinder precipitation from the melt is greatly enhanced, yielding a high GFA of the alloy [26]. Here, in the search for good glass formers, three binary eutectics $Zr_{44}Cu_{56}$, $Zr_{51}Al_{49}$ and $Zr_{64}Ni_{36}$ were chosen due to their low melting points and line compound products for eutectic reactions. Therefore, based on proportionally mixing binary deep eutectics, the composition C_{am} in the quaternary Zr–Cu–Ni–Al alloy system can be obtained as follows:

$$C_{am} = x(Zr_{44}Cu_{56}) + y(Zr_{64}Ni_{36}) + z(Zr_{51}Al_{49}) \tag{2}$$

where x, y and z are the coefficients for the three basic units summing up to unity. The atomic ratios of the alloy components can be changed through variation of the coefficients and, consequently, different compositions of the Zr–Cu–Ni–Al system can be obtained.

As the starting point, the initial coefficients x, y and z were all straightforwardly assigned the value 1/3 resulting

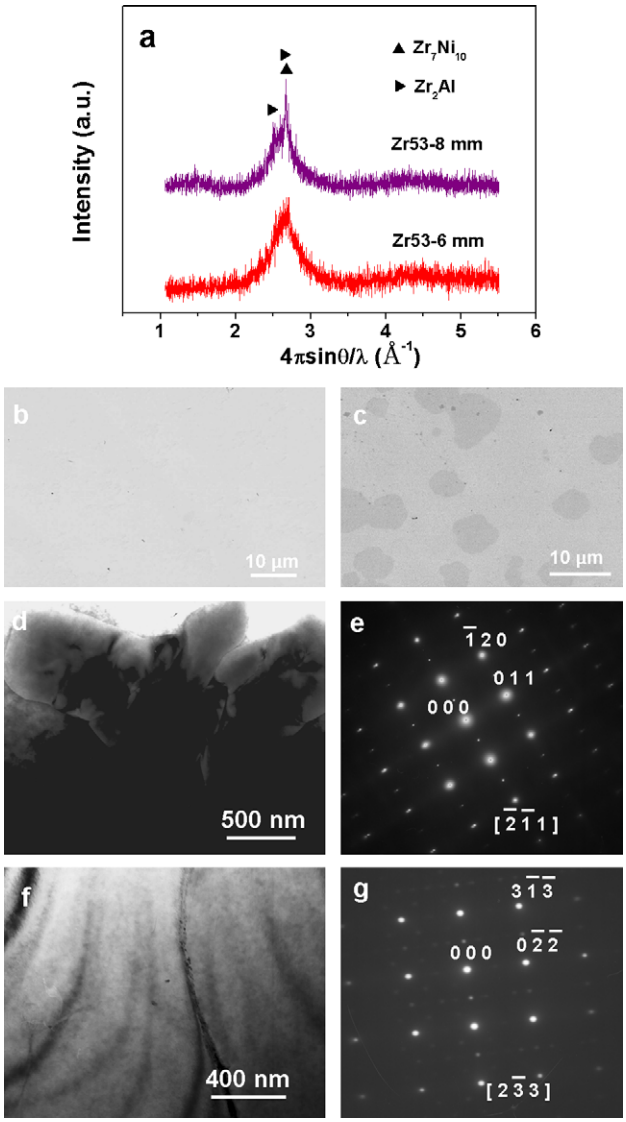

Fig. 1. (a) XRD patterns for as-cast Zr53 samples with the diameters of 6 and 8 mm. (b) SEM-BSE image for the as-cast Zr53 sample with a diameter of 6 mm. (c) SEM-BSE image for the as-cast Zr53 sample with a diameter of 8 mm. (d) Bright-field TEM image and (e) the corresponding selected area electron diffraction pattern for a hexagonal Zr_2Al phase in as-cast Zr53 sample with the diameter of 8 mm. (f) Bright-field TEM image and (g) the corresponding electron diffraction pattern for an orthorhombic Zr_7Ni_{10} phase in as-cast Zr53 sample with the diameter of 8 mm.

with Eq. (2) in $Zr_{53}Cu_{18.7}Ni_{12}Al_{16.3}$ (abbreviated as Zr53). In what follows Zr53 will be designated as the starting composition to modify the quaternary Zr–Cu–Ni–Al alloy compositions, aiming to increase their GFA.

Fig. 1a shows the XRD patterns for the Zr53 alloy with diameters of 6 and 8 mm. As can be seen, the XRD pattern for the 6 mm diameter sample consists of only broad diffraction maxima without any sharp Bragg peak, indicating that this sample is amorphous in structure within the XRD detection limit. Fig. 1b presents the SEM back-scattered

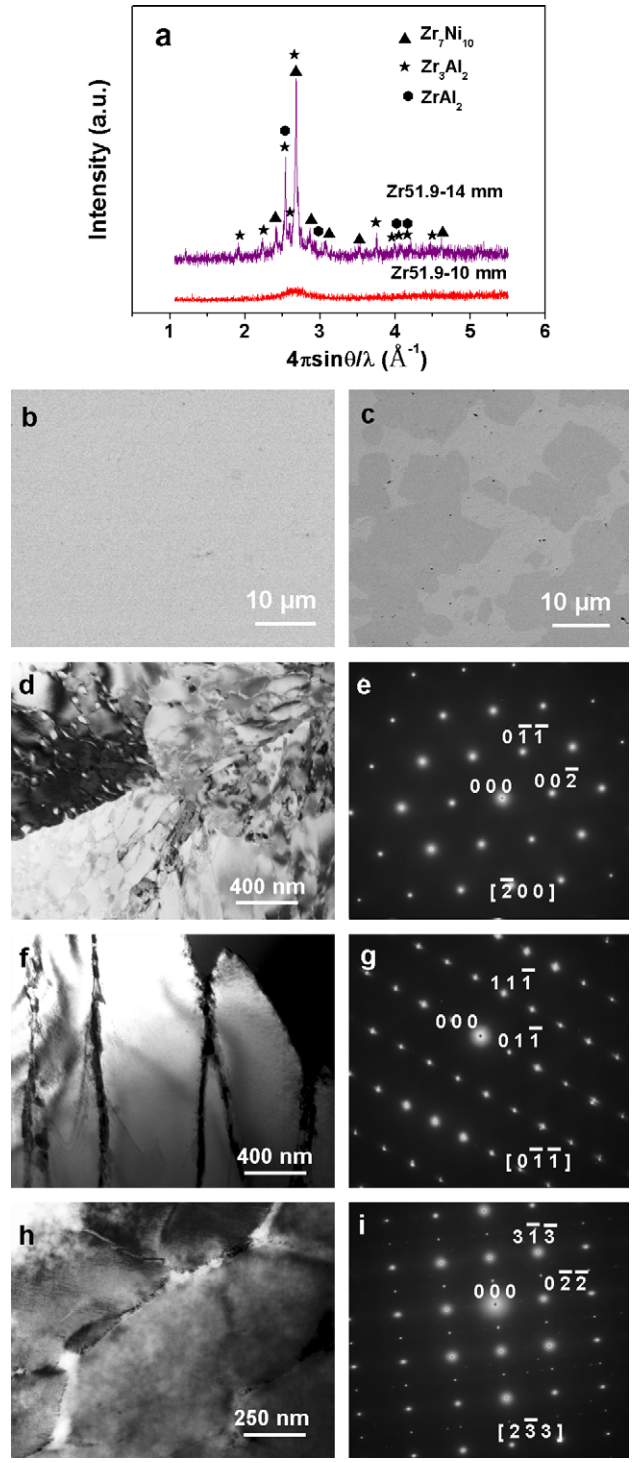

Fig. 2. (a) XRD patterns for as-cast Zr51.9 samples with the diameters of 10 and 14 mm. (b) SEM-BSE image for the as-cast Zr51.9 sample with a diameter of 10 mm. (c) SEM-BSE image for the as-cast Zr51.9 sample with a diameter of 14 mm. (d) Bright-field TEM image and (f) the corresponding selected area electron diffraction pattern for a hexagonal $ZrAl_2$ phase in as-cast Zr51.9 sample with the diameter of 14 mm. (e) Bright-field TEM image and (g) the corresponding selected area electron diffraction pattern for a tetragonal Zr_3Al_2 phase in as-cast Zr51.9 sample with the diameter of 14 mm. (h) Bright-field TEM image and (i) the corresponding selected area electron diffraction pattern for an orthorhombic Zr_7Ni_{10} phase in as-cast 14 mm rod-shaped Zr51.9 sample.

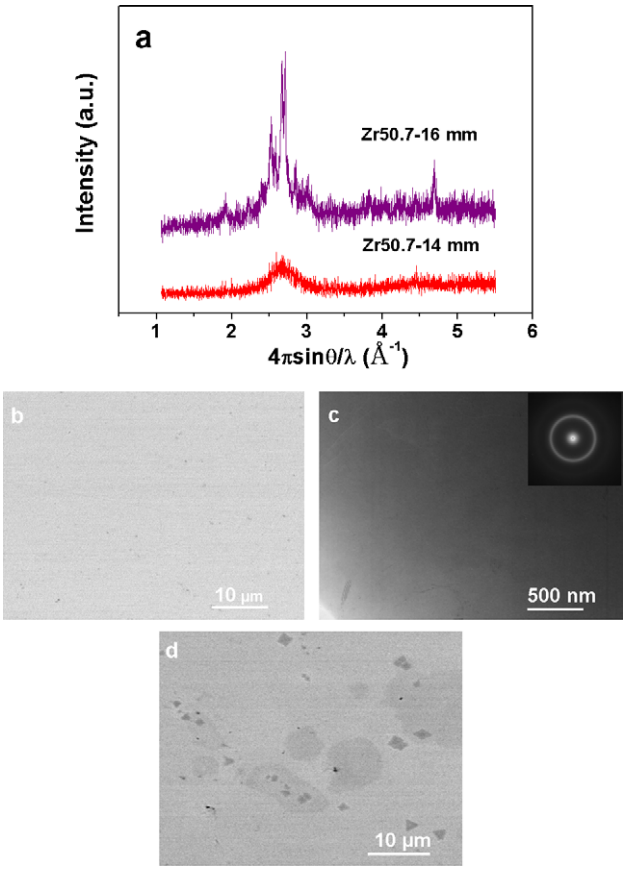

Fig. 3. (a) XRD pattern for the as-cast Zr50.7 samples with a diameters of 14 and 16 mm. (b) SEM-BSE image for the as-cast Zr50.7 sample with a diameter of 14 mm. (c) Bright-field image TEM and corresponding selected area electron diffraction pattern (inset) for the as-cast Zr50.7 sample with a diameter of 14 mm. (d) SEM-BSE image for the as-cast Zr50.7 sample with a diameter of 16 mm.

electron (SEM-BSE) image for the 6 mm diameter Zr53 alloy. There is no contrast of crystalline phases in the sample, confirming that the 6 mm sample of the Zr53 alloy is mostly amorphous. In contrast, the XRD pattern for this alloy (Fig. 1a) of the as-cast rod-shaped sample of 8 mm in diameter exhibits visible crystalline peaks corresponding to Zr_2Al and Zr_7Ni_{10} phases on top of the first amorphous diffraction peak. Fig. 1c shows the SEM-BSE image for 8 mm diameter Zr53 alloy. It can be clearly seen that some crystalline phases are dispersed in the amorphous matrix. Furthermore, these crystalline phases can be identified by TEM observations as the hexagonal Zr_2Al phase ($a = 4.89$ Å, $c = 5.93$ Å) (Fig. 1d and e) and the orthorhombic Zr_7Ni_{10} phase ($a = 9.21$ Å, $b = 9.16$ Å, $c = 12.39$ Å) (Fig. 1f and g). Therefore, for the Zr53 alloy, the maximum diameter of glass formation achievable in the present study is about 6 mm.

These results of the Zr53 alloy show that the precipitation of the Zr_2Al and the Zr_7Ni_{10} phases is the main obstacle to further enhance the GFA of the alloy. In comparison with the element Cu, the contents of Ni and Al are relatively excessive in Zr53, as indicated by the phase analysis. In order to further improve the GFA of this quaternary alloy system without adding an extra element, we reduced the coefficients for the Zr–Ni and the Zr–Al eutectic units in Eq. (2), aiming to suppress the precipitation of Zr_2Al and Zr_7Ni_{10} intermetallics. The coefficients for the binary eutectics $Zr_{64}Ni_{36}$ and $Zr_{51}Al_{49}$ were each decreased to 7/24 (i.e. $y = z = 7/24$) and the coefficient for $Zr_{44}Cu_{56}$, x, was increased to 10/24, leading to a new composition $Zr_{51.9}Cu_{23.3}Ni_{10.5}Al_{14.3}$ (abbreviated as Zr51.9). The microstructure for this alloy was also examined by XRD, SEM and TEM, as shown in Fig. 2. The diffuse diffraction peak in the XRD pattern (Fig. 2a) shows mostly amorphous character of the Zr51.9 alloy with a 10 mm diameter and the corresponding SEM-BSE image (Fig. 2b) demonstrates that there is only a single amorphous matrix in this sample. However, several sharp crystalline peaks superimposed on the broad halo peak are visible in the XRD pattern (Fig. 2a) of the 14 mm sample. The SEM-BSE image (Fig. 2c) also shows that there are some crystalline phases dispersed in an amorphous matrix. TEM observations further confirm that these crystalline phases are the hexagonal $ZrAl_2$ phase ($a = 5.28$ Å, $c = 8.75$ Å) (Fig. 2d and e), the tetragonal Zr_3Al_2 phase ($a = 7.63$ Å, $c = 6.70$ Å) (Fig. 2f and g) and the orthorhombic Zr_7Ni_{10} phase ($a = 9.21$ Å, $b = 9.16$ Å, $c = 12.39$ Å) (Fig. 2h and i) intermetallics. These results indicate that the critical diameter of glass formation for the Zr51.9 alloy can reach up to 10 mm.

In order to suppress the precipitation of Zr_2Al and Zr_7Ni_{10} phases from the Zr53 alloy, decreasing the contents of binary Al-rich eutectics $Zr_{51}Al_{49}$ and Ni-rich $Zr_{64}Ni_{36}$ can significantly enhance the GFA of the Zr–Cu–Ni–Al alloy system, for which the critical diameter can increase from about 6 mm to about 10 mm by minor modification of the coefficients. For the Zr51.9 alloy, the precipitations are still Al-rich and Ni-rich intermetallics. Aiming to further improve the GFA of the Zr–Cu–Ni–Al alloy system, we reduced the coefficients y and z to 6/24, and the coefficient x was increased to 12/24, resulting in a new composition $Zr_{50.7}Cu_{28}Ni_9Al_{12.3}$ (abbreviated as Zr50.7). The XRD pattern (Fig. 3a) of the 14 mm diameter Zr50.7 alloy shows only a broad diffuse halo, indicating that the sample is essentially amorphous. Fig. 3b and c presents the SEM-BSE and TEM images for the 14 mm Zr50.7 alloy, respectively, showing typical amorphous features in agreement with the corresponding XRD result. For the 16 mm Zr50.7 alloy, however, the XRD pattern (Fig. 3a) and the corresponding SEM-BSE (Fig. 3d) shows the precipitation of crystalline phases in this sample. Therefore, for the Zr50.7 alloy, the critical diameter of glass formation is about 14 mm. One can expect that GFA of this alloy system can be further improved by finely tuning the three coefficients x, y and z. The experimental results presented here have already confirmed the feasibility of the method proposed by the authors for efficient search of bulk glass formers.

Fig. 4 shows the DSC and DTA curves obtained from the three Zr–Cu–Ni–Al amorphous alloys. All alloys exhi-

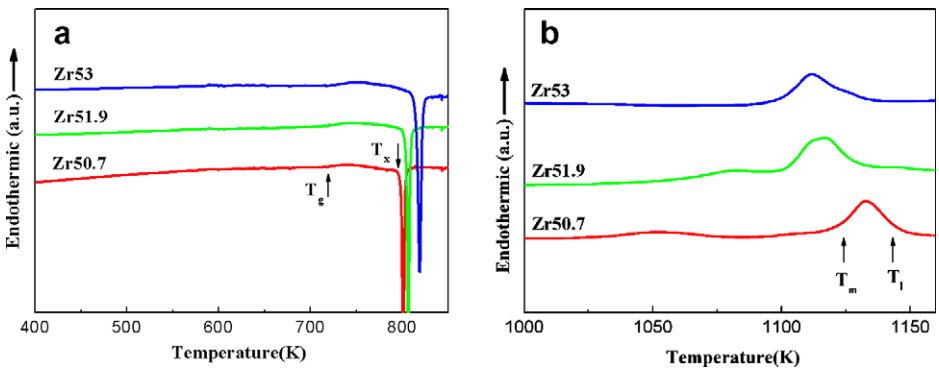

Fig. 4. DSC (a) and DTA (b) curves for as-cast Zr53, Zr51.9 and Zr50.7 bulk amorphous alloys.

Table 1
The new alloy compositions, abbreviations, adjustment of mixing constants, maximum diameter D_{max}, and thermal parameters for the Zr–Cu–Ni–Al alloys.

BMG compositions (abbreviation)	Mixing coefficients	D_{max} (mm)	T_g (K)	T_x (K)	T_l (K)	T_g/T_l
$Zr_{53}Cu_{18.7}Ni_{12}Al_{16.3}$ (Zr53)	$x = 1/3$, $y = 1/3$, $z = 1/3$	6	709	815	1141	0.621
$Zr_{51.9}Cu_{23.3}Ni_{10.5}Al_{14.3}$ (Zr51.9)	$x = 10/24$, $y = 7/24$, $z = 7/24$	10	710	804	1129	0.629
$Zr_{50.7}Cu_{28}Ni_9Al_{12.3}$ (Zr50.7)	$x = 12/24$, $y = 6/24$, $z = 6/24$	14	719	799	1142	0.630

bit an endothermic event characteristic of the glass transition and a distinct supercooled liquid region, followed by an exothermic peak due to crystallization. Table 1 summarizes the maximum diameters, D_{max}, of the glassy samples as well as the corresponding thermal parameters, including the glass transition temperature T_g, the onset crystallization temperature T_x, the liquidus temperature T_l, and the reduced glass transition temperature $T_{rg} = T_g/T_l$ measured at a constant heating rate of 0.33 K s^{-1}. So up to now, as indicated by the values of T_{rg} and D_{max}, which are two powerful criteria reflecting the GFA of amorphous alloys, the alloy Zr50.7 is the best glass former among the three alloys.

4. Discussion

As described in Section 3, an alloy composition with super-high GFA can be obtained by proportionally mixing binary eutectics. Moreover, the glass-forming ability of the alloy system can be substantially enhanced without increasing the component species but by varying sole variation of the relative ratios of the eutectic compositions. In this section, we aim to interpret the GFA for the amorphous alloys obtained and to explore the structural origin of the superior GFA.

4.1. Glass formation and glass-forming ability of the Zr–Cu–Ni–Al alloys

It has been shown that eutectic compositions are the best candidates for glass formation due to their low liquidus temperature T_l and consequently high T_{rg}. Another feature of our method of mixing binary eutectics is that the eutectic reaction products are line compounds. As Shen et al. [26] suggested, if the chemical affinity between the eutectic atomic pairs can be balanced to a certain degree, the atomic rearrangement to form crystalline phases during cooling of a melt is rather difficult, resulting in a pronounced increase in the GFA of the material. In this work, we preferred to choose binary eutectics $Zr_{44}Cu_{56}$, $Zr_{64}Ni_{36}$ and $Zr_{51}Al_{49}$, which are line eutectics with low melting points, as the three preliminary units. It is expected that a balance for the chemical affinity between the eutectic atomic pairs can be achieved by proportionally mixing the corresponding binary eutectic compositions.

Although some of the physics behind our method remains unclear, numerous alloy compositions created by using it and reported in the literature verify the feasibility, effectiveness and efficiency of this procedure. As shown in Table 2, the multi-component alloy compositions obtained through proportionally combining the binary eutectic pairs between the constituent elements are very close to those of BMGs reported in the literature [10,11,40–47]. Such a simple method opens an alternative avenue towards better understanding of the physical meaning of glass formation and a means for finding glass-forming alloy compositions.

Because phase selection inevitably occurs upon cooling, either crystalline phases or glassy phases can be the solidification products. It is the competition between the formations of glassy and crystalline phases that controls the GFA of an alloy [20]. Glass formation could be interpreted as the complete suppression of nucleation and growth of crystalline phases. In order to obtain a better glass-forming composition, primary precipitation in the melt should be bypassed no matter what the crystalline phases are, as suggested by Lu et al. [48]. One of the effective approaches to improving the GFA is to suppress the precipitation of crystalline phases through phase competition. Therefore, based

Table 2
Glass-forming alloy compositions obtained through our method and reported in the literature.

Mixing of binary eutectics according to appropriate ratios	Compositions obtained through our new method	Compositions reported in literature [Reference]
$1/3(La_{24}Al_{76}) + 2/3(La_{69}Ni_{31})$	$La_{54}Al_{25.3}Ni_{20.7}$	$La_{55}Al_{25}Ni_{20}$ [38]
$1/5(La_{24}Al_{76}) + 2/5(La_{71}Cu_{29}) + 2/5(La_{69}Ni_{31})$	$La_{60.8}Al_{15.2}Cu_{11.6}Ni_{12.4}$	$La_{62}Al_{15.7}(Cu, Ni)_{22.3}$ [39]
$1/4(Cu_{72}Y_{28}) + 1/3(Mg_{91}Y_9) + 5/12(Cu_{14.5}Mg_{85.5})$	$Mg_{66}Cu_{24}Y_{10}$	$Mg_{65}Cu_{25}Y_{10}$ [40]
$1/3(Cu_{62}Zr_{38} + 1/3(Cu_{46}Zr_{54}) + 1/3(Cu_{73}Ti_{27})$	$Cu_{60.3}Zr_{30.7}Ti_9$	$Cu_{60}Zr_{30}Ti_{10}$ [41]
$1/10(Zr_{76}Ni_{24}) + 1/10(Zr_{38}Cu_{62}) + 1/4(Ti_{76}Ni_{24}) + 11/20(Ti_{27}Cu_{73})$	$Cu_{46.3}Ni_{8.4}Ti_{33.9}Zr_{11.4}$	$Cu_{47}Ni_8Ti_{34}Zr_{11}$ [42]
$3/10(Y_{58}Al_{42}) + 3/10(Y_{68.9}Co_{31.1}) + 2/10(Sc_{43}Al_{57}) + 2/10(Sc_{63}Co_{37})$	$Y_{38.1}Sc_{21.2}Al_{24}Co_{16.7}$	$Y_{36}Sc_{20}Al_{24}Co_{20}$ [43]
$1/2(Pd_{81}P_{19}) + 1/2(Ni_{81}P_{19})$	$Pd_{40.5}Ni_{40.5}P_{19}$	$Pd_{40}Ni_{40}P_{20}$ [44]
$1/2(Pd_{81}P_{19}) + 1/8(Ni_{81}P_{19}) + 3/8(Cu_{84.3}P_{15.7})$	$Pd_{40.5}Ni_{10.1}Cu_{31.6}P_{17.8}$	$Pd_{40}Ni_{10}Cu_{30}P_{20}$ [45]
$1/4(Zr_{76}Ni_{24}) + ½(Zr_{38}Cu_{62}) + 1/4(Zr_{70}Al_{30})$	$Zr_{55.5}Cu_{31}Ni_6Al_{7.5}$	$Zr_{55}Cu_{30}Ni_5Al_{10}$ [11]
$1/2(Zr_{76}Ni_{24}) + 1/4(Zr_{38}Cu_{62}) + 1/4(Zr_{70}Al_{30})$	$Zr_{65}Cu_{15.5}Ni_{12}Al_{7.5}$	$Zr_{65}Cu_{17.5}Ni_{10}Al_{7.5}$ [10]

on the concept of phase competition, we designed the three compositions $Zr_{53}Cu_{18.7}Ni_{12}Al_{16.3}$, $Zr_{51.9}Cu_{23.3}Ni_{10.5}Al_{14.3}$ and $Zr_{50.7}Cu_{28}Ni_9Al_{12.3}$, by varying the ratios of the three eutectic units, $Zr_{44}Cu_{56}$, $Zr_{51}Al_{49}$ and $Zr_{64}Ni_{36}$. It is envisioned that through this adjustment the chemical affinities of the four components Zr, Cu, Ni and Al get balanced much better in the melt prior to solidification and then the precipitation of these competing phases is suppressed, which resultantly improved the GFA of this Zr–Cu–Ni–Al alloy system.

For the purpose of comparison, other known Zr-based amorphous alloys with excellent GFA were also fabricated under identical experimental condition in our lab. Table 3 lists their critical diameters (D_{max}) and thermal parameters. Fig. 5 shows the XRD patterns obtained from the as-cast Zr-based alloys with different diameters. It is evident that, among the Zr–Cu–Ni–Al quaternary alloy systems, the Zr50.7 alloy created in this work exhibits the highest GFA, which is even comparable to that of the quinary $Zr_{51}Ti_5Ni_{10}Cu_{25}Al_9$ alloy.

4.2. Structural origin of the superior GFA of Zr–Cu–Ni–Al alloys

Metallic glasses are basically frozen liquids with amorphous atomic structures formed through bypassing crystallization during solidification [23,48]. There usually exist certain heredities between the structures of a metallic liquid and the corresponding amorphous counterpart, i.e., the atomic structure of a glass has the randomness similar to that of a liquid [2].

In order to determine the structural origin of the GFA for our new Zr–Cu–Ni–Al alloys, synchrotron radiation HEXRD investigations were carried out and the results are given in Fig. 6a showing the as-measured diffraction patterns for the three alloys, straightly matching the XRD patterns of the amorphous samples in Figs. 1–5a but showing much better statistics accuracy and extending further into Q-space. Further, the data was normalized to background and form factors to obtain the scattering function $S(Q)$, as shown in Fig. 6b, which shows subtle but important differences among the three curves. The intensities $I(Q)$ and the scattering functions $S(Q)$ for the three samples are in accordance with each other and the second peaks are accompanied with shoulders, as indicated by the arrow in Fig. 6b.

Kelton et al. [49] carried out the first in situ X-ray scattering studies on electrostatically levitated metallic supercooled liquid, and considered that the shoulder peaks on the $S(Q)$–Q curves can be taken as a signal of the presence of icosahedral short-range order (ISRO). Similar results were also obtained by Kim et al. [50]. It has also been experimentally proven that five-fold local symmetry exists in simple metallic liquids [51]. Similarly, we also treat the shoulders here as a fingerprint of the presence of ISRO. The difference is that our results were obtained in the glass state and not in the supercooled liquid. However, as discussed above, a glassy structure is the inheritance of the corresponding supercooled liquid [2]. Therefore, we consider that this stable ISRO structurally hinders atomic diffusion to form the crystalline nuclei, enhancing the GFA of this alloy system.

Basically a Fourier transformation from $S(Q)$ leads to the atomic pair distribution function (PDF), as shown in

Table 3
The critical sizes (D_{max}), achieved under the condition of our lab, and the thermal parameters for Zr-based BMGs of this study and previously reported.

Amorphous alloy systems with the corresponding abbreviation [Reference]	D_{max} (mm)	T_g (K)	T_x (K)	T_l (K)	T_g/T_l
$Zr_{50.7}Cu_{28}Ni_9Al_{12.3}$ (Zr50.7) [this study]	14	719	799	1116	0.630
$Zr_{65}Cu_{17.5}Ni_{10}Al_{7.5}$ (Zr65) [10]	<6	657	736	1168	0.563
$Zr_{55}Cu_{30}Ni_5Al_{10}$ (Zr55) [11]	<10	682	745	1104	0.618
$Zr_{57.5}Cu_{27.3}Ni_{6.5}Al_{8.7}$ (Zr57.5) [24]	<14	651	755	1124	0.596
$Zr_{51}Ti_5Cu_{25}Ni_{10}Al_9$ (Zr51) [19]	14	680	724	1002	0.679
$Z_{r41.2}Ti_{13.8}Cu_{12.5}Ni_{10}Be_{22.5}$ (Zr41.2) [7]	>18	623	672	996	0.626

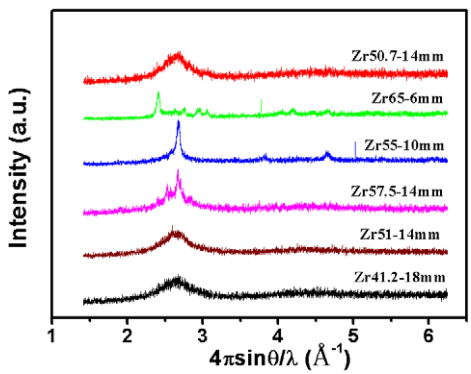

Fig. 5. XRD patterns for selected Zr-based amorphous alloy alloys with different diameters.

Fig. 6c, which presents relative sharp correlation peaks below 7–8 Å and smooth oscillations above. While the sharp peaks reveal high order in form of clusters of the corresponding size, long-range correlations behave like a typical fully amorphous material designating the coordination spheres with the maxima of the oscillations. Fig. 6d and e shows magnified parts of the interesting regions in Fig. 6c. The first correlation peak splits into two sub-peaks located at around 2.7 and 3.2 Å stemming from a discrete distribution of nearest neighbor atoms. Moreover, with the sequence of Zr53, Zr51.9 and Zr50.7, the height of the first sub-peak increases in cost of the second sub-peak which is a trend to shorter bond lengths with the variation of atoms. Accordingly, since the clusters are built by smaller units, the correlation spheres, i.e. the oscillation maxima at larger distances, Fig. 6e, shift to smaller values.

In liquid and amorphous materials, structural information is mainly distracted from the radial distribution function (RDF) $J(r)$ or the pair distribution function (PDF) $g(r)$. Both functions are composed of several independent partial pair distribution functions by weight [52,53]. In order to obtain more structural information from the experimental curves, decomposition must be carried out, as shown in the following equation [54]:

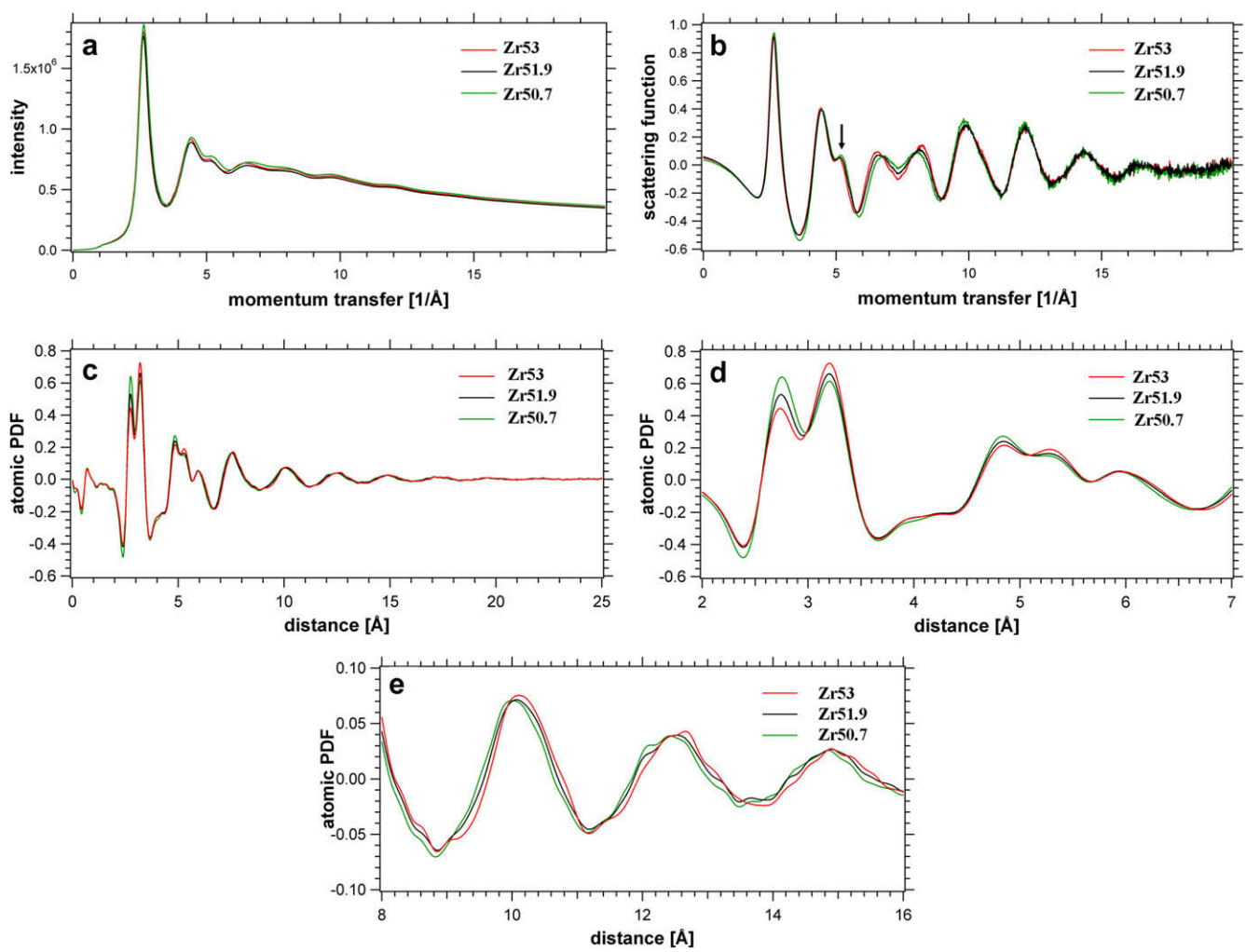

Fig. 6. Synchrotron radiation high-energy X-ray diffraction results for the as-cast Zr53, Zr51.9 and Zr50.7 bulk amorphous alloys: (a) intensity-quantum transfer ($I(Q)$–Q) curves; (b) scattering function-quantum transfer ($S(Q)$–Q) curves; (c) atomic pair distribution functions, and the zoomed view of the near range (d) and the far range (e) of (c).

$$g(r) = \sum_{i,j} w_{i,j} g_{i,j}(r) \tag{3}$$

where $g(r)$ is the total PDF, $g_{i,j}(r)$ is the partial pair distribution function between the ith and the jth atomic pairs, $w_{i,j}$ is the weight factor of $g_{i,j}(r)$ in $g(r)$, with

$$w_{i,j} = c_i c_j f_i f_j \Big/ \left(\sum_i c_i f_i \right)^2 \tag{4}$$

where c_i and f_i are the atomic concentration and scattering length of the ith atom in the alloys, respectively. However, $g_{i,j}(r)$ for the multi-component alloy system is difficult and ambiguous to calculate, even though some simplifications to the decomposition of PDF have been introduced by Ma et al. [53]. As a result, here we just obtained the weight factor through Eq. (4), as suggested by Jiang et al. [8,55]. Since the scattering function $S(Q)$ has been implicitly corrected for the Q-dependence of $f(Q)$ $f_i = f_i(Q = 0)$ is set to the atomic number of the corresponding ith element because of the high-energy of the incident X-ray. The bond lengths and weight factors of Zr53, Zr51.9 and Zr50.7 are listed in Table 4. As can be seen, with the enhancement of GFA in the three alloys, the weight factors of Cu–Cu, Cu–Ni, Al–Cu and Zr–Cu also increase, but other factors decrease.

Comparing the compositions of $Zr_{53}Cu_{18.7}Ni_{12}Al_{16.3}$ (Zr53), $Zr_{51.9}Cu_{23.3}Ni_{10.5}Al_{14.3}$ (Zr51.9) and $Zr_{50.7}Cu_{28}Ni_9Al_{12.3}$ (Zr50.7), it can be seen that, in the sequence of Zr53, Zr51.9 and Zr50.7, the concentrations of Zr, Ni and Al gradually decrease, whereas the concentration of Cu exhibits an inverse trend. In other words, among the three alloys studied, introducing more Cu atoms into the Zr–Cu–Ni–Al alloy system makes the alloy melt more stable, consequently improving the GFA of alloy system. Qualitatively comparing the bond lengths and weight factors for all the atomic pairs, only for the Zr–Zr atomic pair, the bond length 3.16 Å is close to the second nearest neighbor sub-peak's site on the PDF curve, about 3.25 Å. The weight factor decreases with increasing the GFA of the three alloys. This is consistent with the decreasing of the second nearest neighbor sub-peak in the atomic PDF curves for the three investigated alloys. With respect to the first nearest neighbor sub-peaks around 2.7 Å in the atomic PDF, if we consider the bond lengths of these atomic pairs and their weight factors, the increase in the first nearest neighbor sub-peak can be explained by the increment of shorter bonded Al–Cu atomic pairs.

Although at present the atomic structures in amorphous alloys still remain mysterious, it has been discovered that besides the dense random packing from the macroscopic view, there are also nanometer-scale short-range order clusters and medium-range order clusters packing in the material [56–58]. Based on these perspectives, Miracle [31,32] suggested that inside the multi-component bulk metallic glasses, atoms are efficiently packed. Furthermore, the structures of the amorphous alloys are the results of efficient cluster packing (ECP), as shown in Fig. 7, providing a unique view for understanding the structural origin of BMGs.

Therefore, the GFA of the three alloys can be interpreted according to the ECP model. Miracle [31,32] and Wang et al. [59] treated Zr–Al–(Cu, Ni) alloys as a

Table 4
The bond lengths between atoms and the calculated weight factors of the partial pair distribution functions for Zr53, Zr51.9 and Zr50.7 metallic glasses.

Bond type	Bond length (Å)	Weight factor			Bond type	Bond length (Å)	Weight factor		
		Zr53	Zr51.9	Zr50.7			Zr53	Zr51.9	Zr50.7
Cu–Cu	2.54	0.029	0.044	0.062	Zr–Cu	2.85	0.112	0.134	0.156
Cu–Ni	2.55	0.0176	0.0190	0.0193	Al–Al	2.86	0.003	0.003	0.002
Ni–Ni	2.56	0.011	0.008	0.006	Zr–Ni	2.86	0.069	0.058	0.048
Al–Cu	2.7	0.0111	0.0120	0.0123	Zr–Al	3.01	0.044	0.037	0.031
Al–Ni	2.71	0.007	0.005	0.004	Zr–Zr	3.16	0.436	0.413	0.389

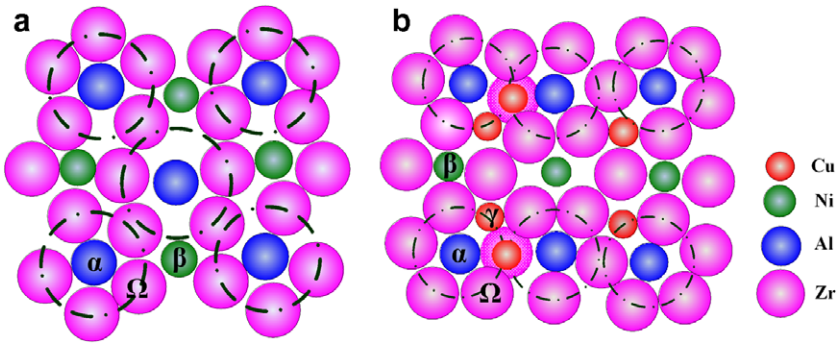

Fig. 7. Schematics of the fcc cluster packing in the efficient cluster packing (ECP) structure for the Zr–Al–(Cu, Ni) bulk amorphous alloy: (a) {100} plane view, and (b) {110} plane view.

pseudo-ternary Ω–α–β alloy system. Here, Ω represents the solvent atom, both α and β represent solute atoms with decreasing atomic radii. The ECP structure is then formed by solute-centered clusters in a way similar to face-centered cubic (fcc) or hexagonal close packing (hcp). For the present work, the ECP structure of Zr–Al–(Cu, Ni) alloy can be represented as $\langle 12,10\rangle_{\mathrm{fcc}}$ in Miracle's nomenclature.

The mixing heats of Zr–Al and Zr–Ni pairs are −44 and −49 kJ mol^{-1}, respectively, which are the most negative values for all atomic pairs in Zr–Cu–Ni–Al alloys [60]. Thus, these pairs can easily form stable short-range order clusters just as Miracle [31,32] and Wang et al. [59] suggested by taking their reduced atomic radii and chemical interactions into account. However, in the three alloys studied here, both the concentration and the atomic radius of Ni are smaller than those of Al. Therefore, Zr–Al can be taken as the α-clusters, while Zr–Ni as the β-clusters for the alloy system studied. Both of these clusters are considered to be stable. The Cu atoms should be inserted into cluster-tetrahedral vacancies to form β_γ site defects in this structure. However, it will only give a composition of $Zr_{60}Al_{10}(Ni,Cu)_{30}$ which is different from any of our compositions. In comparison with our compositions, the concentration of Zr atoms is relatively higher and that of the Al atoms is lower in $Zr_{60}Al_{10}(Ni,Cu)_{30}$. Therefore in order to coincide with our compositions, other Ω site defects caused by Cu and Al must be introduced into this model, besides the β_γ site defects caused by Cu and Ni.

After introducing more Cu and Al atoms into this structure, these two elements occupy all of the γ sites and some Ω sites to form β_γ and β_Ω defects, as shown in Fig. 7a and b. In this structure, all Cu atoms occupy γ sites forming β_γ defects and some Cu atoms substitute Zr atoms forming β_Ω defects. Both of these defects contribute Al–Cu, Al–Ni and Ni–Cu atom pairs to the atomic PDF. Because of the low Ni concentration and the unique bond lengths of the Ni–Al and Ni–Cu atomic pairs, both of their contributions to the PDF can be neglected. Therefore, as mentioned above, only the Al–Cu atomic pairs prominently affect the first nearest neighbor sub-peaks, the height of which increases with increasing Cu atoms. On the other hand, when more Cu atoms are introduced into the alloy system to substitute Zr atoms, the number of Zr–Zr atomic pairs decreases, leading to a lessening of the height of the second nearest neighbor sub-peak, as described previously. Therefore, by substituting Cu atoms for Zr in this Zr–Cu–Ni–Al alloy, the atomic packing efficiency increases in the order Zr53, Zr51.9 and Zr50.7, leading to the corresponding gradual enhancement of the GFA.

As Wang et al. [59] pointed out, the maximum solute concentration in the ECP model is closely correlated with the strains created by the atomic packing. In fact, the atomic radii of Ni and Cu are very similar, while the cluster-tetrahedral site γ is very small. Larger elastic strain will be induced in the β_γ defect when introducing such a large Cu atom into this small γ site. We see that these defects are compressive and inevitably accompanied by high elastic energy in the ECP structure. The structure erupts when the elastic energy exceeds the critical value. Therefore, the substitution of small Cu atoms for large Zr, as illustrated in Fig. 7b, is a very comfortable path to ease the strain, stabilizing the ECP structure of the three alloys and enabling the formation of BMG with a high GFA.

5. Conclusions

(1) Bulk metallic glasses in the Zr–Cu–Ni–Al alloy system with different GFA were identified through proportional mixing of binary eutectics $Zr_{44}Cu_{56}$, $Zr_{51}Al_{49}$ and $Zr_{64}Ni_{36}$. An initial composition $Zr_{53}Cu_{18.7}Ni_{12}Al_{16.3}$ (Zr53) with a critical size of 6 mm was obtained by following the formula $1/3(Zr_{44}Cu_{56}) + 1/3(Zr_{64}Ni_{36}) + 1/3(Zr_{51}Al_{49})$. In order to further improve the GFA of the quaternary alloy system without adding an additional element, ratios of these binary eutectics were adjusted, aiming to suppress the formation of Zr–Al and Zr–Ni competing crystalline phases. Consequently, the glass-forming alloys of $Zr_{51.9}Cu_{23.25}Ni_{13.5}Al_{12.25}$ (Zr51.9) with a critical size of 10 mm and $Zr_{50.7}Cu_{28}Ni_9Al_{12.3}$ (Zr50.7) with a critical size of 14 mm were achieved.

(2) Synchrotron radiation high-energy X-ray diffraction results indicate the first peaks in the atomic pair distribution function curves for all the Zr–Cu–Ni–Al amorphous alloys split into two sub-peaks. Combined with Miracle's ECP atomic structure model, we considered that the substitution of small Cu atoms for large Zr atoms in the alloys studied provides a reasonable means for stabilizing the ECP structure, ensuring an increased GFA.

Acknowledgements

The research was supported by the National Nature Science Foundation of China under Grant Nos. 50771040 and 10732010. The authors acknowledge John Daniels for his assistance in measurements at the European Synchrotron Radiation Facility, Grenoble, France, Milen Gateshki for advice and support in the PDF analysis, and Q.K. Jiang for his assistance in calculating atomic pair weight factors.

References

[1] Johnson WL. MRS Bull 1999;24:42.
[2] Wang WH, Dong C, Shek CH. Mater Sci Eng R 2004;44:45.
[3] Ashby MF, Greer AL. Scripta Mater 2006;54:321.
[4] Greer AL, Ma E. MRS Bull 2007;32:611.
[5] Telford M. Mater Today 2004;7:36.
[6] Inoue A. Acta Mater 2000;48:279.
[7] Peker A, Johnson WL. Appl Phys Lett 1993;63:2342.
[8] Jiang QK, Wang XD, Nie XP, Zhang GQ, Ma H, Fecht HJ, et al. Acta Mater 2008;56:1785.

[9] Inoue A, Yokoyama Y, Shinohara Y, Masumoto T. Mater Trans 1994;35:923.
[10] Inoue A, Zhang T, Nishiyama N, Ohba K, Masumoto T. Mater Trans 1993;34:1234.
[11] Inoue A, Zhang T. Mater Trans 1996;37:185.
[12] Xing LQ, Ochin P, Harmelin M, Faudot F, Bigot J, Chevalier JP. Mater Sci Eng A 1996;220:155.
[13] Greer AL. Science 1995;267:1947.
[14] Klement W, Willens R, Duwez P. Nature 1960;187:869.
[15] Johnson WL. Prog Mater Sci 1986;30:81.
[16] Egami T. Mater Sci Eng A 1997;226–228:261.
[17] Prabhat KG, Miracle DB. Acta Mater 2007;55:4507.
[18] Poon SJ, Shiflet GJ, Guo FQ, Ponnambalam V. J Non-Cryst Solids 2003;317:1.
[19] Chen W, Wang Y, Qiang J, Dong C. Acta Mater 2004;51:1899.
[20] Ma D, Tan H, Wang D, Li Y, Ma E. Appl Phys Lett 2005;86:191906.
[21] Shi LL, Xu J, Ma E. Acta Mater 2008;56:3613.
[22] Cao H, Ma D, Hsieh KC, Ding L, Stratton WG, Voyles PM, et al. Acta Mater 2006;54:2975.
[23] Turnbull D. Contemp Phys 1969;17:437.
[24] Highmore RJ, Greer AL. Nature 1989;339:363.
[25] Lu ZP, Li Y, Ng SC. J Non-Cryst Solids 2000;270:103.
[26] Shen J, Zou J, Ye L, Lu ZP, Xing DW, Yan M, et al. J Non-Cryst Solids 2005;351:2519.
[27] Lu ZP, Shen J, Xing DW, Sun JF, Liu CT. Appl Phys Lett 2006;89:071910.
[28] Liang WZ. Doctoral dissertation, Harbin Institute of Technology, China; 1998.
[29] Yang YJ, Xing DW, Li CP, Wei SD, Sun JK, Shen QK. Mater Sci Eng A 2007;448:15.
[30] Wang D, Tan H, Li Y. Acta Mater 2005;53:2969.
[31] Miracle DB. Nature Mater 2004;3:697.
[32] Miracle DB. Acta Mater 2006;54:4317.
[33] Liss KD, Bartels A, Schreyer A, Clemens H. Text Microstruct 2003;35:219.
[34] Tschentscher T, Suortti P. J Synchrotron Radiat 1998;5:286.
[35] Yeoh LR, Liss KD. dataRring. Lucas. Heights, Australia, Bragg Institute, ANSTO; 1998.
[36] Petkov V. J Appl Cryst 1989;22:387.
[37] Eckert J, Kühn U, Mattern N, Reger-Leonhard A, Heilmaier M. Scripta Mater 2001;44:1587.
[38] Saida J, Matsushita M, Li C, Inoue A. Mater Sci Eng A 2001;304–306:338.
[39] Wang WH, Bian Z, Wen P, Zhang Y, Pan MX, Zhao DQ. Intermetallics 2002;10:1249.
[40] Inoue A, Nakamura T, Sugita T, Zhang T, Masumoto T. Mater Trans 1993;34:351.
[41] Tan H, Zhang Y, Ma D, Feng YP, Li Y. Acta Mater 2003;51:4551.
[42] Kim SG, Inoue A, Masumoto T. Mater Trans 1990;31:929.
[43] Inoue A, Zhang W, Zhang T, Kurosaka K. Acta Mater 2001;49:2645.
[44] Lin XH, Johnson WL. J Appl Phys 1995;78:6514.
[45] Guo FQ, Poon SJ, Shiflet GJ. Appl Phys Lett 2003;83:2575.
[46] Kui HW, Greer AL, Turnbull D. Appl Phys Lett 1984;45:615.
[47] Inoue A, Nishiyama N, Kimura H. Mater Trans 1997;38:179.
[48] Lu ZP, Ma D, Liu CT, Chang YA. Intermetallics 2007;15:253.
[49] Kelton KF, Lee GW, Gangopadhyay AK, Hyers RW, Rathz TJ, Rogers JR. Phys Rev Lett 2003;90:195504.
[50] Kim TH, Gangopadhyay AK, Xing LQ, Lee GW, Shen YT, Kelton KF, et al. Appl Phys Lett 2005;87:251924.
[51] Reichert H, Klein O, Dosch H, Denk M, Honkimäki V, Lippmann T, et al. Nature 2000;408:839.
[52] Luborsky FE. Amorphous metallic alloys. London: Butterworths; 1983.
[53] Ma D, Stoica AD, Yang L, Wang XL, Lu ZP, Neuefeind J, et al. Appl Phys Lett 2007;90:211908.
[54] Yang L, Chao Y, Saksl K, Franz H, Sun LL, Wang WK, et al. Appl Phys Lett 2004;84:4998.
[55] Jiang QK, Zhang GQ, Yang L, Wang XD, Saksl K, Franz H, et al. Acta Mater 2007;55:4409.
[56] Sheng HW, Luo WK, Alamgir FM, Bai JM, Ma E. Nature 2006;439:419.
[57] Hufnagel TC, Brennan S. Phys Rev B 2003;67:014203.
[58] Miracle DB, Egami T, Flores KM, Kelton KF. MRS Bull 2007;32:629.
[59] Wang AP, Wang JQ, Ma E. Appl Phys Lett 2007;90:121912.
[60] Takeuchi A, Inoue A. Mater Trans 2005;46:2817.